Autler-Townes splitting and acoustically induced transparency based on Love waves interacting with a pillared metasurface

Yuxin Liu, Abdelkrim Talbi, El Houssaine El Boudouti, Olivier Bou Matar, Philippe Pernod, Bahram Djafari-Rouhani

Autler-Townes Splitting and Acoustically Induced Transparency Based on Love Waves Interacting with a Pillared Metasurface

Yuxin Liu,[1,*] Abdelkrim Talbi,[1] El Houssaine El Boudouti,[2] Olivier Bou Matar,[1] Philippe Pernod,[1] and Bahram Djafari-Rouhani[1]

[1] *Univ. Lille, CNRS, Centrale Lille, ISEN, Univ. Valenciennes, UMR 8520 – IEMN & LIA LICS/LEMAC, F-59000 Lille, France*

[2] *LPMR, Department of Physics, Faculty of sciences, University Mohammed I, 60000 Oujda, Morocco*

(Received 11 March 2019; revised manuscript received 14 May 2019; published 27 June 2019)

Autler-Townes splitting (ATS) and electromagnetically induced transparency (EIT) are similar phenomena but distinct in nature. They have been widely discussed and distinguished by employing the Akaike information criterion (AIC). However, such work is lacking in acoustic systems. In this work, the interaction of Love waves with a two-line pillared metasurface is numerically investigated by the finite-element method. An acoustic analog of ATS, Fabry-Perot resonance, and cavity modes are first demonstrated in two lines of identical pillars by varying the distance between the pillar lines. By detuning the radius of one line of pillars, Fabry-Perot resonance along with two different pillar resonances give rise to the acoustic analog of EIT (AIT) when the distance between the pillar lines is a multiple of half wavelength. ATS and AIT formula models are used to fit the transmission spectra, showing good agreements with numerical results. The quality of the fit models is quantitatively evaluated by resorting to the AIC. We show that theoretical and analytical discrimination between ATS and AIT are methodologically complementary. These results should have consequences for potential acoustic applications such as wave control, and the design of metamaterials and biosensors.

DOI: 10.1103/PhysRevApplied.11.064066

I. INTRODUCTION

Electromagnetically induced transparency (EIT) is a well-known physical effect in atomic systems that arises because of quantum destructive interferences between two excitation pathways to an upper atomic level [1]. Steep dispersion and low absorption take place in a sharp transparency window, which makes it very attractive for plenty of potential applications in slowing light, enhancing optical nonlinearity, and data storage [2–4]. Autler-Townes splitting [5] (ATS), which is the field-induced splitting of the optical response, is not associated with interference effects and has been described as an incoherent sum of two Lorentzians [6]. EIT and ATS may phenomenologically look similar, but they are different in nature, one being a quantum interference and the other a linear ac Stark effect. EIT and ATS were first observed in quantum and atom systems [5,7]. In recent years, classic analogs of EIT and ATS have attracted increasing interest in platforms such as photonics [8–10], optomechanics [11–13], plasmonics [14–16], and metamaterials [17–19]. Many discussions have been devoted to their easily confused absorption or transmission spectra [8,20–22]. Besides their differences in the physical mechanisms, the Akaike information criterion (AIC) has been proposed to quantitatively discern EIT from ATS [20], and the transition from ATS to EIT is thereby carried out [23]. A crossover from EIT to ATS has been shown to exist in hot molecules [24], and in open ladder systems [25]. In acoustics, the analog of EIT, also referred to as AIT, has been investigated in different structures [26–30], but the analog of ATS and its comparison with AIT was only recently reported [31]. Additionally, the distinction and transition between the acoustic analog of ATS and AIT has not been quantitatively investigated before.

In the last two decades, phononic crystals have received increasing attention [32–38]. They exhibit Bragg and/or hybridization band gaps to achieve control of elastic wave propagation, and apply to various aspects such as rf communications [34,39,40], acoustic isolators [41–43], sensors [38,44–46], thermoelectric materials [37,47,48], and metamaterials [36,49–53]. The phononic pillared metasurface is a recently proposed structure stemming from pillared phononic crystals. It consists of a single or a line of pillars on top of a slab, with which one can thoroughly investigate pillar resonant properties. The pillar size, periodicity, and slab thickness are all subwavelength scaled [54,55]. Several studies have been devoted to the interaction of pillared metasurfaces with Rayleigh waves [56] and Lamb waves [57,58], but no work has been done on Love waves, which

*yuxin.liu@phd.ec-lille.fr

are shear horizontal (SH) polarized surface acoustic waves (SAWs). Love waves propagate in a thin guiding layer deposited on the surface of a semi-infinite substrate, and is therefore considered a compromise between Rayleigh waves and Lamb waves: compared with Rayleigh waves, Love waves are well confined to the surface because of the thin guiding layer in which they propagate. In contrast to Lamb waves, Love waves exhibit device toughness since the guiding layer is deposited on the semi-infinite substrate. A Love-wave-based pillared metasurface is therefore suitable for use in wave control, sensors, and design of metamaterials. Moreover, Love waves can excite pillar torsional mode [59], which is impossible to excite by Rayleigh waves and Lamb waves (S0 and A0) [57]. In addition to the above qualities, their compatibility with liquid environment [45,60] makes Love waves ideal candidates for biosensor applications.

In this work, the interaction of Love waves with a two-line Ni pillar-based metasurface is investigated on a SiO_2/ST quartz structure. Firstly, torsional mode in one line of cylindrical Ni pillars is demonstrated to be well excited by Love waves and gives rise to a sharp transmission dip due to a destructive interference. Secondly, the acoustic analog of ATS and cavity modes for Love waves are first demonstrated in two lines of identical pillars by varying the distance between the pillar lines. ATS appears when the distance is smaller than the half wavelength and a strong coupling is aroused between the pillar lines. Fabry-Perot (FP) resonance exists at the positions where the distance between the pillar lines is a multiple of half wavelength. The proximity of Fabry-Perot resonance with pillar torsional mode gives rise to the cavity modes with transmission enhancement at the edges of the dip induced by the pillars. Thirdly, the radius of one line of pillar is modified to detune the pillar resonant frequency. In the pillar coupling region, the coupling effect decreases with the increase of radius mismatch. When the distance between the pillar lines is a multiple of half wavelength, Fabry-Perot resonance along with the two different pillar resonances give rise to the AIT resonance. Then, ATS and AIT phenomena are first fitted respectively with corresponding formula models, showing good agreements. The AIC is then used to quantitatively evaluate the quality of the fit models, showing consistent results for the ATS and AIT cases, and the transition from ATS to AIT by increasing the distance between the pillars is illustrated. The AIT phenomenon is shown to be periodic due to the periodicity of Fabry-Perot resonance. The band structures and the transmission spectra are calculated with the finite-element method (FEM, COMSOL Multiphysics®).

II. UNIT CELL MODEL

The acoustic metasurface is constituted of two-pillar lines deposited on a bilayered matrix, of which the unit cell is shown in Fig. 1. The matrix is a 2.4-μm-height silica guiding layer ($\rho = 2200$ kg/m^3, $E = 70$ GPa, $\nu = 0.17$) that covers a 40-μm-high 90ST-cut quartz substrate [Euler angles $= (0°, 47.25°, 90°)$, LH 1978 IEEE], which has been rotated 90° around the z axis from the ST-cut quartz, to be able to generate fast pure SH waves ($c_{\mathrm{SH,sub}} = 5000$ m/s) by the electric field. The shear wave velocity in the silica film is 3438 m/s, less than that in the 90ST-cut quartz substrate, indicating the existence of Love waves. This structure is chosen since it has been experimentally validated for Love waves [61]. The guiding layer thickness is subwavelength since only the fundamental Love mode exists to avoid physical complexity. The period along the y axis is $a = 2$ μm. Two cylindrical Ni pillars on the silica film have a radius of $r_1 = r_2 = 0.2a$ and a height of $h = 0.6a$. The distance between the centers of the two pillars is denoted by d. The inclusions are chosen because of their strong contrast in density and elastic constants with regard to the matrix. However, similar results can also be obtained by using other materials such as gold or diamond. The length of the unit cell L is $20a$ to ensure a decoupling between the unit cells. Floquet periodic boundary conditions are applied along the x and y directions. The bottom of the substrate is assumed fixed. Love waves propagate along the x axis (i.e., the y axis of the ST-cut quartz), where Rayleigh waves cannot be generated [62] due to a zero electromechanical coupling factor in the substrate. The surfaces of the pillars coincide with the plane $z = 0$. The wavelength normalized energy depth (σ) [63] is calculated to select the surface modes:

$$\sigma = \frac{\iiint_{\mathcal{D}} \frac{1}{2} T_{ij} S_{ij}^{*}(-z)\,dxdydz}{\lambda \iiint_{\mathcal{D}} \frac{1}{2} T_{ij} S_{ij}^{*}\,dxdydz}, \tag{1}$$

where T_{ij} is the stress and S_{ij} the strain. The star symbol (*) means the complex conjugate. $-z$ denotes that we integrate in the whole domain of the unit cell $\mathcal{D}$. λ is the wavelength. This formula works well for a relatively large k where the

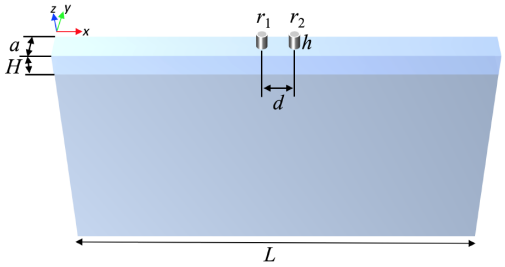

FIG. 1. Unit cell of two lines of cylindrical Ni pillars on the SiO_2 film deposited on a 90ST-cut quartz. The period is a along the y direction. Love waves propagate along the x axis. $r_1 = r_2 = 0.2a$, $h = 0.6a$, $H = 2.4$ μm, $L = 20a$, $a = 2$ μm.

wave speed is less than the SH wave velocity of the substrate. For a relatively small k (with wave speed greater than the SH wave velocity of the substrate), which corresponds to a large λ, we fix λ to $4a$. Surface modes have a $\sigma < 1$. The σ can filter out the bulk modes as well as the plate modes that appear in our finite-depth substrate, which is supposed to be semi-infinite for Love waves.

SAWs include SH-type SAWs and Rayleigh-type SAWs. The SH ratio is calculated to distinguish the displacement components:

$$\eta_{\mathrm{SH}} = \frac{\iiint_{\mathcal{D}} u_{\mathrm{SH}} u_{\mathrm{SH}}^* dxdydz}{\iiint_{\mathcal{D}} (u_x u_x^* + u_y u_y^* + u_z u_z^*) dxdydz}, \tag{2}$$

where u_x, u_y, and u_z are respectively the displacement along the x, y, z directions. u_{SH} is the SH displacement component that can be expressed as $u_x \cos\theta - u_y \sin\theta$, which is perpendicular to the wave vector $\mathbf{k}$. θ is the angle between $\mathbf{k}$ and the y axis such that $\tan\theta = k_x/k_y$. In our case, $\mathbf{k} = \mathbf{k}_x$ and $u_{\mathrm{SH}} = u_y$.

III. RESONANT PROPERTIES OF A SINGLE-PILLAR LINE

Firstly, we study the resonant properties of the unit cell with only one pillar, which corresponds to a metasurface with a single-pillar line. The dispersion curves or band structure of SH modes ($\eta_{\mathrm{SH}} > 0.5$) in the x direction is shown in Fig. 2(b). The X point is the irreducible Brillouin-zone limit of the unit cell in the x direction. The mode colors are determined by their σ values. The modes in red are well confined to the surface, and can therefore be excited by Love waves. Certain modes become pink as they are less confined to the surface. Two hybridization band gaps are observed respectively in the frequency range [177.3, 183.1] MHz and [501.8, 503.3] MHz, indicated in blue, which originates from the coupling of local resonant pillar modes and the SH SAW. Note that in the frequency range [100, 600] MHz, the wavelength ranges from 6.8 to 48.8 μm. Therefore, our structure is indeed a metasurface with subwavelength-scaled pillar size, periodicity, and guiding layer thickness.

The transmission spectra is calculated by simulating the same dispersive SAW device introduced in our preceding works [63,64], which has been validated by experiment. The model consists of two parts of aluminum interdigital transducers (IDTs) with the unit cell located between IDTs. This device model is periodic along the y direction. Other lateral sides and the bottom are assumed fixed. The input IDT is given a $V_0 = 1V$ harmonic voltage signal. The output is measured by averaging the voltage difference between odd and even electrodes. Dissipation is neglected in the results shown in the manuscript. However, its effect is discussed in Appendix A supporting the validity of the presented features. The width of the electrodes

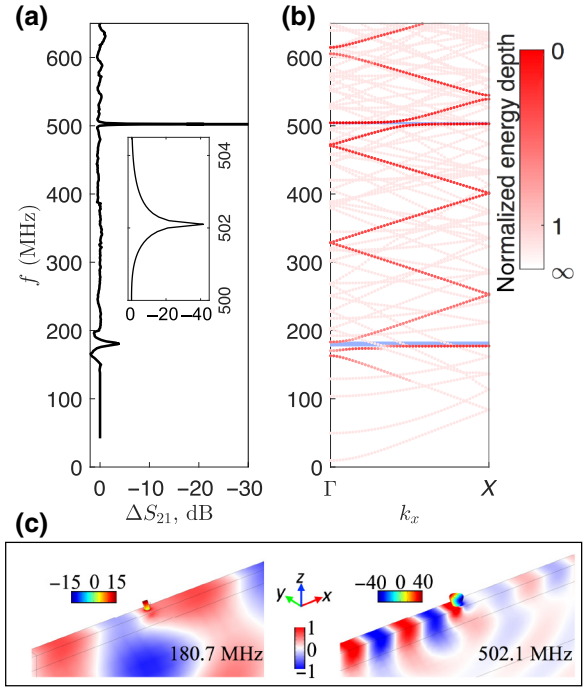

FIG. 2. (a) Transmission spectrum of Love waves propagating through a single-pillar line. Inset is the enlargement of the torsional-mode-induced dip. (b) Band structure of SH modes in Γ X direction for the unit cell of a single-pillar line. The red-white colors denote the normalized energy depth. A mode in red can be excited by Love waves. (c) u_y component of the displacement fields for two local resonant pillar modes. The amplitudes in the pillar are normalized to the maximum amplitude in the SiO_2 film. $r = 0.2a$. $h = 0.6a$, $a = 2$ μm.

of IDTs L_{IDT} is updated for every frequency in the spectrum according to the relation $L_{\mathrm{IDT}} = (\lambda/4) = (v/4f)$. v is the velocity of Love waves for $H = 2.4$ μm, resulting from the basic dispersion relation of Love waves. That is, each frequency corresponds to a single wavelength. The frequency responses are then normalized by that of the matrix (without pillar), referred to as relative transmissions ΔS_{21}. Figure 2(a) shows the transmission spectrum of the single-pillar line. It can be seen that the transmission spectrum corroborates well with the band-structure prediction. The displacement fields and the deformations at the two dips are shown in Fig. 2(c). Due to their large SH component ratio, as well as the exclusive generation of SH waves by the electric field, we only show the transverse component u_y. The amplitude in the pillar is normalized to that in the matrix and is indicated beside the pillar. The two dips correspond to the pillar's intrinsic bending and torsional modes, respectively. The torsional-mode-induced transmission dip is better attenuated, since the excited torsional motion leads to, on the side opposite to the incident wave, a wave of identical amplitude and opposite phase, which is responsible for a destructive interference. To further confirm this mechanism, the emitted wave (Em) is

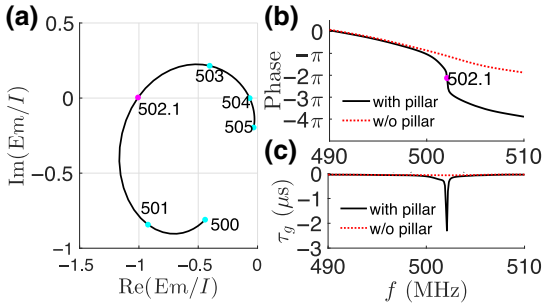

FIG. 3. (a) Complex plot of the normalized emitted waves in the frequency range [500, 505] MHz. The rose dot corresponds to the transmission dip at 502.1 MHz. (b) Phase of total transmitted waves. Red dotted line denotes the reference phase (incident waves without pillar). (c) Group delay time of the transmitted waves with and without pillar.

calculated by subtracting the incident waves I (transmitted waves on the bare matrix without pillar) from the totally transmitted waves T: $\mathrm{Em} = T - I$. Em is then normalized by I. Figure 3(a) is the complex plot of the normalized emitted wave in the frequency range [500, 505] MHz around the torsional mode. The rose dot corresponds to the dip at resonant frequency of 502.1 MHz. This mode falls at point $(-1, 0)$, which refers to the same amplitude with a phase shift of 180° with respect to the incident waves. This results in a destructive interference and a strong attenuation in transmission. The phase shift of full transmitted waves is shown in Fig. 3(b). Red dotted lines represent the incident waves. The dip corresponds to a π change in phase with respect to the incident waves. The phase shift is 0 (2π) before (after) the resonant frequency, meaning that the transmitted waves are in phase with the incident waves when they deviate from the resonant frequency. The corresponding phase derivative or group delay time τ_g of the transmitted waves is shown in Fig. 3(c), with $\tau_g = d\phi/d\omega$, where ϕ denotes the phase and $\omega = 2\pi f$ is the angular frequency. The waves are delayed at the resonant frequency. It can be seen that the resonance is characterized by a rapid variation of phase and amplitude.

By scaling the model in the same proportion, we can obtain the same dimensionless frequency $\omega a/c_{\mathrm{SH,sub}}$ of a mode. Since the pillar intrinsic mode is almost independent of the periodicity, one can also tune the pillar mode frequency only by modifying the pillar size. Note that this frequency needs to be within the allowable operating range of the materials.

IV. TWO LINES OF IDENTICAL PILLARS: AUTLER-TOWNES SPLITTING AND CAVITY MODE

Transmission spectra are then calculated around the torsional-mode frequency for two lines of identical pillars. In addition to our intuitively predicted transmission dip, different phenomena appear when we gradually increase the distance d between the pillar lines. When $d < 1.4a$ [Fig. 4(a)], a coupling effect arises between the pillar lines, causing a lifting of frequency degeneracy of the pillar torsional mode, and the original transmission dip splits into two dips with a transparency window in the middle, referred to as the acoustic analog of ATS. The coupling becomes stronger when d gets smaller, as shown in

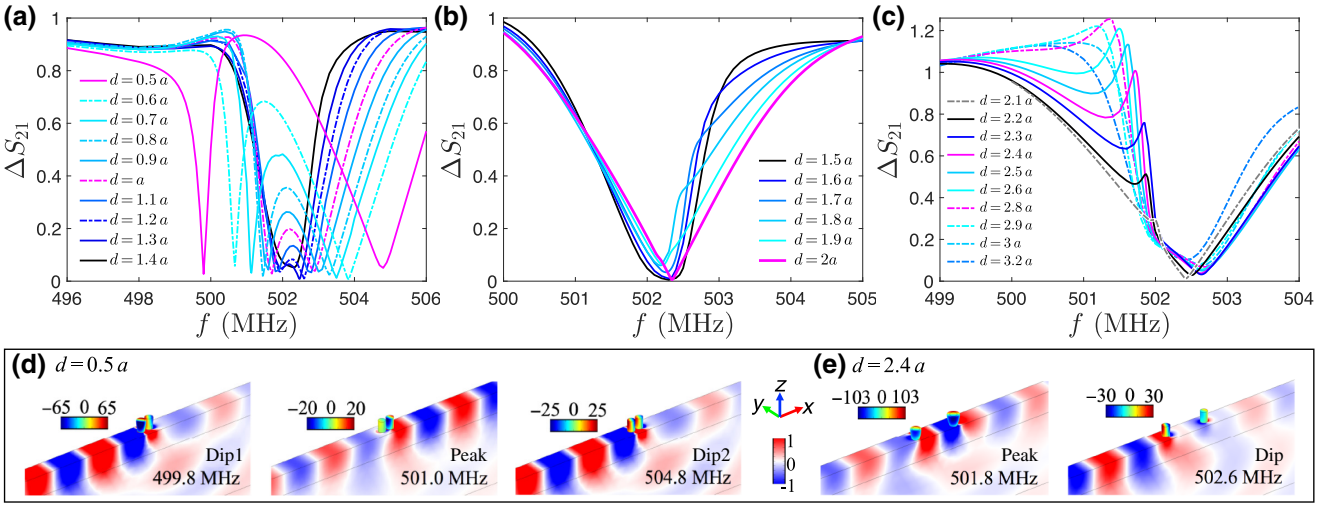

FIG. 4. Transmission spectrum of Love waves propagating through the two identical pillar lines around the resonant frequency of torsional mode at 502.1 MHz with different central distance d: (a) presents the lifting of degeneracy and the apparition of Autler-Townes splitting with the decrease of d; (b) shows the redshift of cavity mode by increasing d when $d < 2a$; (c) presents the appearance of a cavity-mode peak when $d > 2a$; (d),(e) are the displacement fields u_y at the dips and peaks for $d = 0.5a$ and $2.4a$, respectively. $r_1 = r_2 = 0.2a$, $a = 2$ μm.

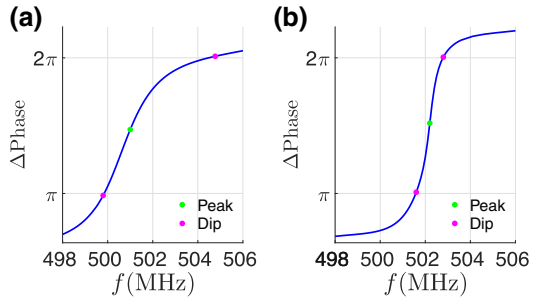

FIG. 5. Pillar phase differences for ATS in the case of (a) $d = 0.5a$ and (b) $d = a$. Rose and green dots correspond to transmission dips and peaks, respectively. $r_1 = r_2 = 0.2a$, $a = 2\ \mu$m.

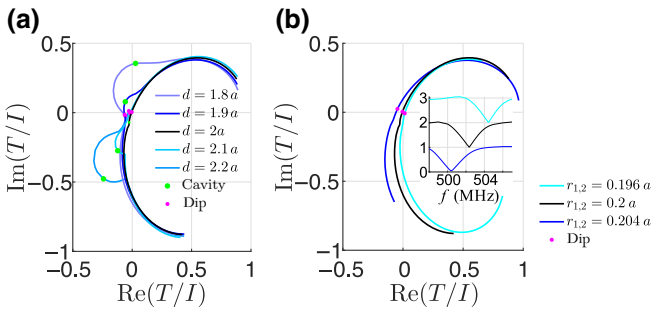

FIG. 6. (a) Complex plots of the normalized transmissiosn in the frequency range [500, 505] MHz for d varies from $1.8a$ to $2.2a$. Rose and green marks correspond to the dip and cavity-mode frequencies, respectively. $r_1 = r_2 = 0.2a$. (b) Complex plots of the normalized transmissions for $d = 2a \approx \lambda/2$ when all the pillars' radius vary from $0.196a$ to $0.204a$. Inset shows the transmission spectra of corresponding curves.

Fig. 4(a). Note that the pillar coupling also depends on the pillar mass. Therefore, the distance limit $1.4a$ can be detuned by changing the pillar size (radius or height). The displacement fields u_y at the dips and peak for $d = 0.5a$ are shown aside in Fig. 4(d). It is found that the largest amplitude is located in the pillars for dip1 at 499.8 MHz. The two pillars are in opposite phase at dip1 frequency and in-phase at dip2 frequency, which is a feature of the ATS resonance that can be confirmed by calculating the phase difference between the two pillars. Since the pillars are in torsional mode in the range of measurement, all the points on the side of the pillar that faces the incident waves are in phase. The phases of u_y on the wave-facing sides of the two pillars are probed. The cases of $d = 0.5a$ and $d = a$ are shown as examples in Figs. 5(a) and 5(b). Rose and green dots correspond to transmission dips and peaks, respectively. It can be seen that the two pillars have a phase difference of π at the first dip, meaning that they are 180° out of phase. The phase difference is 2π at the second dip, indicating that they are in phase. This reveals that the pillar vibrations are symmetrical at the dip1 frequency and asymmetrical at the dip2 frequency. We think this behavior leads to different quality factors of the two dips.

Since we work around 500 MHz with a Love-wave velocity v around 4200 m/s, the wavelength $\lambda = v/f$ is therefore around 8.4 μm. $d \approx 2a$ ($a = 2\ \mu$m) indicates a distance around $\lambda/2$ corresponding to the Fabry-Perot resonance. This resonance is almost invisible in the transmission spectrum when it matches the pillar torsion mode, since the waves are almost totally reflected. However, when we change the distance between pillars around $\lambda/2$, the proximity of FP resonance with the pillar mode gives rise to the cavity modes at the two edges of the dip, as shown in Figs. 4(b) and 4(c). In these cases, the two pillars act like partial reflectors, and the normally incident waves are multiply reflected to produce multiple transmitted waves with path difference equal to $n\lambda$, where n is an integer. In this way, constructive interference occurs, leading to a resonant enhancement. The two pillars along with the guiding layer between them become a cavity to confine the waves. Nevertheless, in the transmission spectra, the behaviors for $d < 2a$ [Fig. 4(b)] are less marked than that for $d > 2a$ [Fig. 4(c)], where peaks rise at the lower edge of the dip, and give rise to Fano-like resonance line shapes. However, we have verified that it can not be fitted by a Fano-type formula. The displacement fields u_y at the peak and dip for $d = 2.4a$ are shown aside in Fig. 4(e), since the transmission curve for $d = 2.4a$ presents the most confined peak. At the peak frequency, large amplitudes are observed for the three parts of the cavity (two pillars and the guiding layer in between). This behavior is different from that of ATS, the largest amplitude in the pillars occurs at the peak where the waves in the guiding layer are highly confined in the cavity.

To show more clearly the transition of the cavity mode with respect to the dip when d changes, we draw the complex plots of the normalized transmissions in Fig. 6(a). The cavity mode is manifested as an additional perturbation on the original ellipse. Since the phase changes clockwise, it can be seen that the cavity mode passes the dip as d increases. When the cavity mode approaches the dip, the perturbation decreases. For $d = 2a$, the cavity mode coincides with the FP resonance and becomes almost invisible. Additionally, we can see that the behaviors for $d < 2a$ and for $d > 2a$ are quite similar, with the perturbation frequency either larger or smaller than the dip frequency.

Figure 6(b) shows the complex plots of the normalized transmissions of Love waves for $d = 2a$ when we change the radius of both pillars from $0.196a$ to $0.204a$, indicating a shift in pillar resonant frequency. It is found that the cavity mode remains almost invisible, i.e., still coincides with the FP resonance. That is because the distance between pillars corresponding to the FP resonance is almost unchanged in our range of measurement (from 498

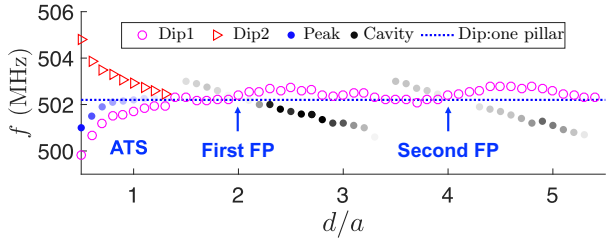

FIG. 7. Dip, peak, and cavity-mode frequencies as functions of the distance d between two identical pillar lines. Blue dotted line is the dip frequency of a single-pillar line. ATS appears in the coupling region of $d < 1.4a$. The first and second Fabry-Perot resonances fall at $d = \lambda/2$ and λ, respectively. $r_1 = r_2 = 0.2a$, $a = 2\ \mu$m.

to 506 MHz), i.e., $\lambda/2$ is always around $d = 2a$. Therefore, when we change the pillar vibration frequency, we obtain the parallel cavity modes for the same value of d.

To give an overview of the resonance behaviors, the dip and peak frequencies for different d are shown in Fig. 7. The blue dotted line is the dip frequency of the single-pillar line. It can be seen that the pillar-coupling-induced ATS is in the region $d < 1.4a$, where the two dips are mismatched with the single-pillar resonant frequency. This coupling disappears when d exceeds $1.4a$, and only one dip (quasizero transmission) remains. This dip matches the single-pillar resonant frequency except when the cavity modes appear below (upon), the dip frequency shifts slightly upward (downward). The interaction between the pillars is much stronger for $d/a = 2$ than that for $d/a = 4$. Therefore, the resonances around $d = \lambda$ are too weak to observe. Note that the frequency of the cavity modes changes much slower than that of the FP resonance. The first and second FP resonance exists only in the very closed regions around $d = 2a$ and $4a$, respectively. In these two cases, FP resonances are particular cases of the cavity modes when the later coincide with the dip. In the other regions, one should avoid mixing up the cavity mode with the FP resonance.

V. TWO LINES OF DISSIMILAR PILLARS: AUTLER-TOWNES SPLITTING, CAVITY, AND ACOUSTICALLY INDUCED TRANSPARENCY

Since an increase of pillar radius or height induces a decrease in the torsional-mode frequency, one can gradually tune the position of the dip by modifying the pillar size. Here we modify the pillar radius as an example since the radius is easier to tune in the experimental process.

In the case below, the second pillar radius r_2 is tuned from $0.195a$ to $0.205a$, while the first pillar radius r_1 is fixed to $0.2a$. Figure 8 shows the transmission spectra of Love waves propagating through the two dissimilar pillar lines for different d that remains unchanged for each case. Let us notice that the curves for different r_2 are shifted vertically with respect to each other. Dotted blue and rose lines denote the dip positions for a single line of pillars with radius equal to r_1 and r_2, respectively. Figure 8(a) corresponds to the case $d = 0.5a$, where the coupling between the pillars is so strong that the two dips stay all the way mismatched with their corresponding single-pillar dip positions. When d gets larger, the coupling becomes weaker: Fig. 8(b) corresponds to the case $d = a$. It is found that this coupling decreases with the increase of radius mismatch. In the case of $r_2 = 0.195a$ and $0.205a$, each dip almost coincides with the corresponding resonant frequency of one single pillar. In order to show the anticrossing lines of ATS for $d < 1.4a$, we plotted in Fig. 9 the dip frequencies for different d as functions of r_2. It can be seen that with the increase of pillar distance, the anticrossing lines get closer to the crossing line (for $d = 1.4a$), and that each anticrossing line will rejoin its individual pillar resonant frequency when the radius mismatch is sufficiently large. This means the pillar-coupling effect

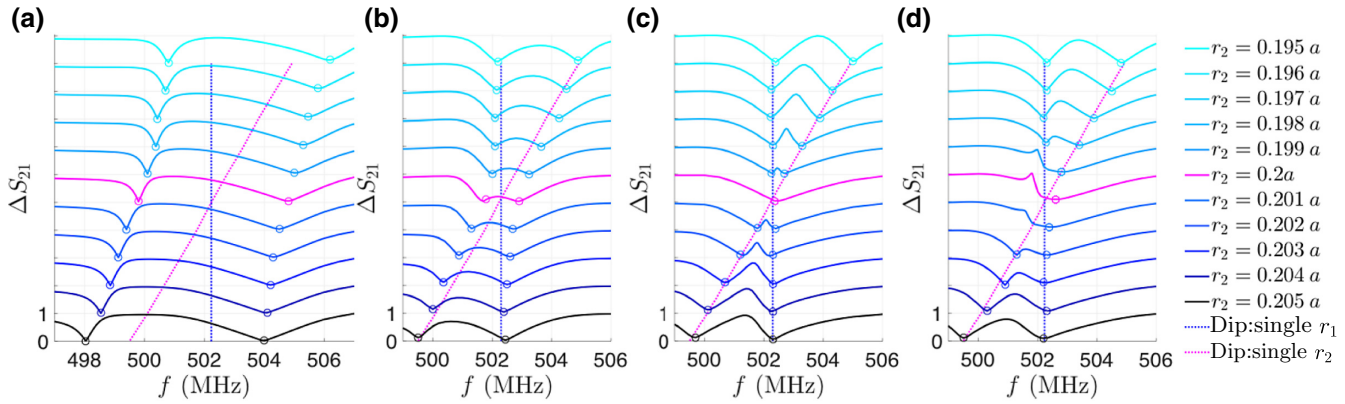

FIG. 8. Transmission spectra of Love waves for $d =$ (a) $0.5a$, (b) a, (c) $2a$, (d) $2.4a$ when gradually changing the radius of the second pillar r_2 from $0.195a$ to $0.205a$. The transmission spectra associated with the different values of r_2 are shifted vertically with respect to each other by one unit. The radius of the first pillar r_1 is fixed to $0.2a$. $a = 2\ \mu$m.

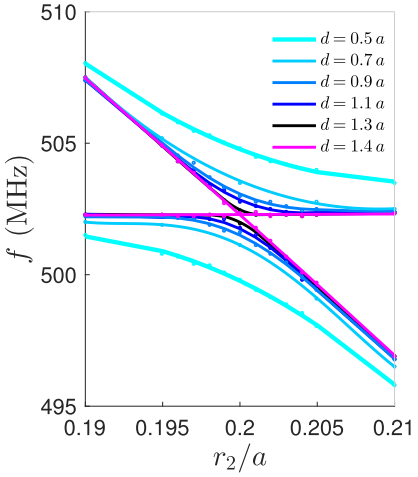

FIG. 9. Anticrossing lines for ATS when $d < 1.4a$. Dip frequencies for different d as a function of the second pillar radius r_2. r_1 is fixed to $0.2a$. $a = 2\ \mu$m.

decreases when their distance or/and their radius difference increases.

For $d = 2a$ as shown in Fig. 8(c), two pillars with different radii give rise to two dips with a transparency window in the middle. These peaks have a narrower line shape compared with the cases of ATS (see also Fig. 11). Each dip is consistent with the corresponding dip frequency of one single pillar since no more coupling exists, which means each of them originates from the individual pillar's torsional mode. The displacement fields u_y for $r_2 = 0.202a$ are presented in Fig. 10. It can be seen that each dip corresponds to a large amplitude in a single pillar, indicating the attenuation of transmission at each pillar's resonant frequency due to the destructive interferences. The peak corresponds to a Fabry-Perot resonance since d is close to $\lambda/2$. The two detuned pillar modes act as two partial reflectors and are hence able to support the constructive interference of the FP resonance, where large amplitudes are observed for the three parts of the cavity (two pillars and the guiding layer in between). This three-resonance system-induced transparency window is referred to as the acoustic analog of electromagnetically induced transparency, also called acoustically induced transparency (AIT). The peak rises and gets wider with the increase of radius difference. As for $d = 2.4a$ shown in Fig. 8(d), where a cavity-mode peak is observed for the two identical pillars, it is found that with the increase of pillar-radius mismatch, the peak confinement decreases and dip1 becomes evident for $r_2 = 0.198a$ and $0.202a$. Compared with the case of $d = 2a$ [Fig. 8(d)], the peak between two dips is less confined due to the redshift of cavity mode with respect to the pillar resonant frequency. Note that AIT requires a well-excited resonance between the two dips. Therefore, in the case of $d = 2.4a$, the transparency window is only two dips resulting from the different resonant frequencies of two pillars.

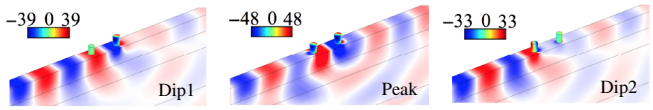

FIG. 10. Displacement field u_y at the dips and peak for AIT in the case of $d = 2a$. The two pillars differ in radius with $r_2 = 0.202a$ and $r_1 = 0.2a$. $a = 2\ \mu$m.

The transmission spectra of AIT are similar with those of ATS, however, they originate from different mechanisms. ATS appears only when the two pillars are coupled to each other, and exists even when the two pillars are identical. AIT appears when d is out of the pillar-coupling region and only when the two pillars are different. The pillars and the cavity interact at the peak. Moreover, AIT requires a clearly identified three-level resonant system, which is not the case for ATS.

Besides the different mechanisms related to ATS and AIT as presented above, corresponding analytical formulas of ATS and AIT for transmission spectra can be used to fit the numerical data to better distinguish these different transparency windows. The transmission curves for ATS can be written as the sum of two separate inverse Lorentzian profiles representing the two dips, while the transmission for AIT is expressed as the difference of a broad Lorentzian profile and a narrow one with a similar

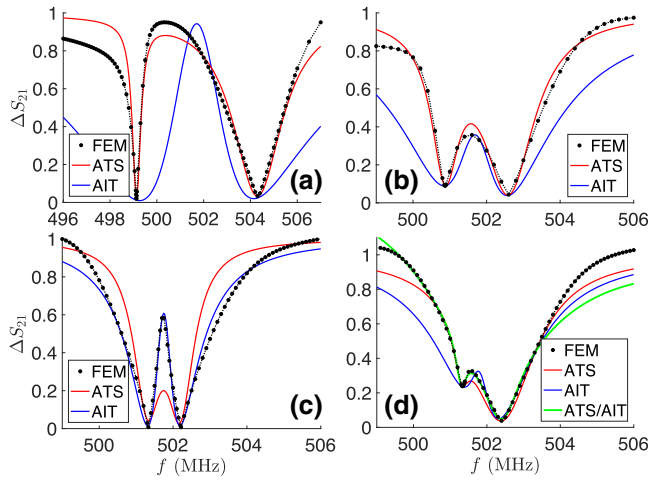

FIG. 11. Transmission spectra and model fits of ATS and AIT, for $r_1 = 0.2a$, $r_2 = 0.202a$, and $a = 2\ \mu$m. Numerical data (black dots) are presented together with the best fits of functions T_{ATS} (red lines) and T_{AIT} (blue lines). For (a) $d = 0.5a$ and (b) $d = a$, T_{ATS} fits the numerical data better than T_{AIT}. (c) For $d = 2a$, T_{AIT} fits the numerical data better than T_{ATS}. (d) For $d = 2.4a$, $T_{\mathrm{ATS/AIT}}$ (green line) can be used to fit the numerical data whereas T_{ATS} and T_{AIT} do not fit well.

central frequency [8,22]:

$$T_{\mathrm{ATS}} = 1 - \frac{C_1(\Gamma_1/2)^2}{(f\ -\delta_1)^2 + (\Gamma_1/2)^2} - \frac{C_2(\Gamma_2/2)^2}{(f\ -\delta_2)^2 + (\Gamma_2/2)^2}, \tag{3}$$

$$T_{\mathrm{AIT}} = 1 - \frac{C_+(\Gamma_+/2)^2}{(f\ -\delta_c - \epsilon)^2 + (\Gamma_+/2)^2} + \frac{C_-(\Gamma_-/2)^2}{(f\ -\delta_c)^2 + (\Gamma_-/2)^2}, \tag{4}$$

where C_1, C_2, C_+, C_- are the amplitudes of the Lorentzian profiles, Γ_1, Γ_2, Γ_+, Γ_- are their FWHM. δ_1, δ_2, δ_c are the central frequencies with ϵ denoting a possible slight shift on δ_c. Γ_1, Γ_2, δ_1, δ_2, and δ_c can be directly taken from the transmission spectra.

In an intermediate state, the transmission spectra can be fitted by a transition formula that considers both the features of ATS and AIT:

$$T_{\mathrm{ATS/AIT}} = 1 - \frac{C_a(\Gamma_a/2)^2}{(f\ -\delta_1)^2 + (\Gamma_a/2)^2} - \frac{C_b(\Gamma_b/2)^2}{(f\ -\delta_2)^2 + (\Gamma_b/2)^2} - \frac{(f\ -\delta_1)C_d(\Gamma_d/2)^2}{(f\ -\delta_1)^2 + (\Gamma_d/2)^2} + \frac{(f\ -\delta_2)C_e(\Gamma_e/2)^2}{(f\ -\delta_2)^2 + (\Gamma_e/2)^2}, \tag{5}$$

where C_a, C_b, C_d, C_e, Γ_a, Γ_b, Γ_d, Γ_e are parameters to be determined. Note that this formula can also be used to fit the ATS and AIT cases.

Figure 11 shows the numerical data (black dots) together with the best-fit functions T_{ATS} (red lines) and T_{AIT} (blue lines) for the four values of d in Fig. 8, which stand for strong coupling ATS, weak coupling ATS, AIT and intermediate states, respectively, in the case of $r_2 = 0.202a$ and r_1 fixed to $0.2a$. The best-fit functions are determined by resorting to the least-squares method, that is, by searching the fit parameters that minimize the sum of squared errors between numerical data χ and the fit function:

$$\sum(\chi_i - F_i)^2, i \in [1, N], \tag{6}$$

where N is the number of values calculated by FEM. F_i is the value of T_{ATS} or T_{AIT} corresponding to each data frequency. It can be seen that, as expected, for $d = 0.5a$ and a where coupling exists between the pillars, T_{ATS} fits the numerical data much better than T_{AIT}. Whereas for $d = 2a$, T_{AIT} fits the numerical data better than T_{ATS}. For $d = 2.4a$, both T_{ATS} and T_{AIT} do not fit the numerical data well. In this case, $T_{\mathrm{ATS/AIT}}$ (green line) fits the data better.

By fitting the numerical data to the model fits of T_{ATS} and T_{AIT} for different r_2 (r_1 fixed), the relation between the fit parameters and r_2 can be obtained as shown in Fig. 12, where Fig. 12(a) presents the fit parameters of

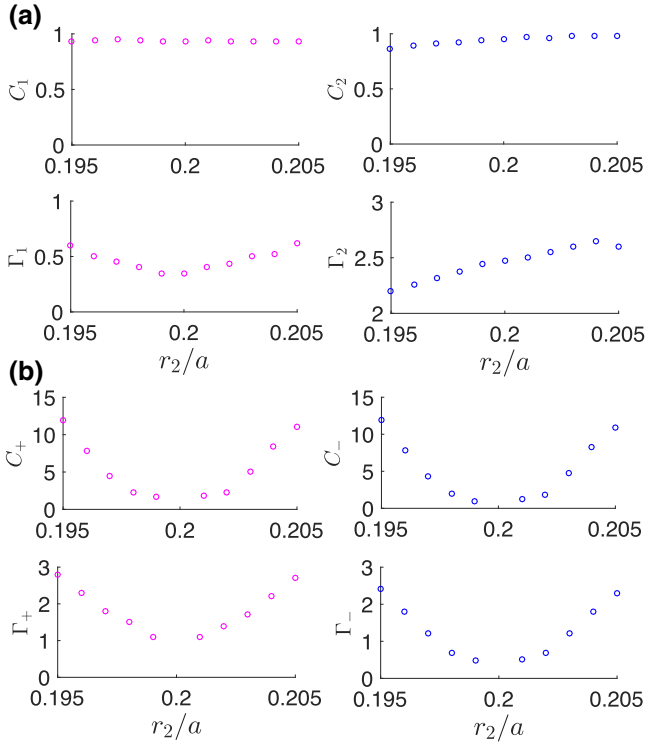

FIG. 12. Fit parameters as functions of r_2/a for (a) $d = 0.5a$ with model fits T_{ATS}; (b) $d = 2a$ with model fits T_{AIT}. $r_1 = 0.2a$, $a = 2\ \mu$m.

the ATS model for $d = 0.5a$ and Fig. 12(b) are those of the AIT model for $d = 2a$. The parameters of the ATS model describing each Lorentzian curve are independent of each other. It can be seen that Γ_1 increases with the increase of radius mismatch while Γ_2 increases with the increase of r_2. We think this is resulting from the symmetrical and asymmetrical vibration of the two pillars at dip1 and dip2, respectively, in the ATS cases. C_1 is relatively stable while C_2 presents a slight tendency to increase. The parameters of the AIT model are related to each other. As can be seen in Fig. 12(b), these four parameters all increase as the radius mismatch increases and are almost symmetrical in our range of measurement. Despite a larger value of Γ_+ compared with Γ_-, C_+ and C_- are almost the same for different r_2.

With the increase of distance between pillars, the transition from ATS to AIT can be quantitatively studied by evaluating the quality of these model fits. The AIC [65] is used to discern AIT from ATS, which provides a method to select the best model from a set of models. This criterion quantifies the amount of information lost, i.e., the degree of unfitness, and is given as $I_j = 2k - 2ln(L_j)$, where $k = 4$ is the number of unknown parameters and L_j the maximum likelihood for the considered models, i.e., j = ATS or AIT. Since we already found the best-fit functions of T_{ATS} and T_{AIT}, it is sufficient to calculate the likelihood of these two

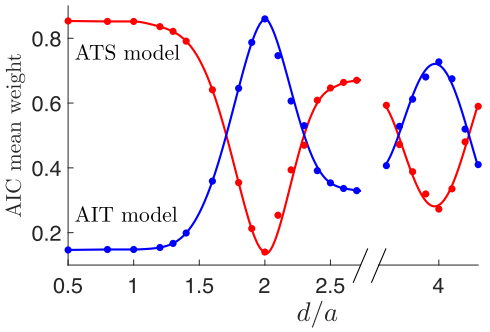

FIG. 13. AIC mean weight as a function of the distance between pillars d for ATS model (red line) and AIT model (blue line), in the case of $r_2 = 0.202a$. $r_1 = 0.2a$, $a = 2\ \mu$m.

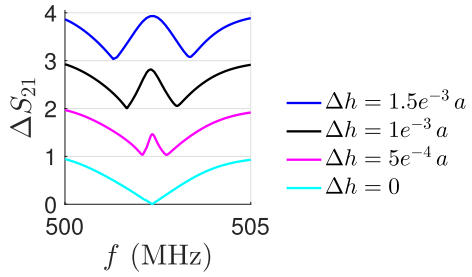

FIG. 14. Transmission spectra of Love waves propagating through the two lines of pillars with different heights, $h_1 = h + \Delta h$ and $h_2 = h - \Delta h$, in the case of $d = 2a$. AIT peak rises and becomes wider with the increase of pillar-height mismatch. $h = 0.6a$, $r_{1,2} = 0.2a$, and $a = 2\ \mu$m.

functions. Then, the AIC weight $W_j = e^{-I_j/2}/\sum_1^N e^{-I_j/2}$ can give the relative likelihood of a candidate model. N is the number of considered models. In our case, $N = 2$ as only two models are involved. Since we have more than one calculated data for each model, we utilize the AIC mean per-point weight [20] $\overline{w}_j = e^{-I_j/2n}/\sum_1^N e^{-I_j/2n}$ to calculate the statistically synthesized likelihood of the candidate model. n is the calculated data number. The AIC mean weight can be rewritten as

$$\overline{w}_{\mathrm{ATS}} = \frac{e^{-I_{\mathrm{ATS}}/2n}}{e^{-I_{\mathrm{ATS}}/2n} + e^{-I_{\mathrm{AIT}}/2n}}, \tag{7}$$

with $\overline{w}_{\mathrm{ATS}} + \overline{w}_{\mathrm{AIT}} = 1$.

Figure 13 shows the AIC mean weight of the ATS and AIT models as a function of the distance between pillars, in the case of $r_2 = 0.202a$ and $r_1 = 0.2a$. It can be seen that, as expected, the AIC mean weight of the ATS model is dominant for the small distance region, which means it is preferable to use the ATS model. When d increases, the AIC mean weight of the AIT model starts to increase as well, and becomes dominant for $d \in [1.8a, 2.2a]$. Since cavity mode is not presented at the peak for $d = 1.8a$, and starts to interact with dip1 for $d = 2.2a$, the AIT is hence in the distance range of $d \in [1.9a, 2.1a]$. When d continues to increase, the AIC mean weight of ATS becomes dominant again until d increases to around $4a$, i.e., the position of the second FP resonance, where we found the second AIT position for $d \in [3.9a, 4.1a]$. The periodicity of AIT, which is a behavior that has not been addressed before in the existing literature, is due to the periodic apparition of the FP resonance. The AIC mean weight of the second AIT region is smaller than that of the first AIT region, since the interaction of the system decreases with the increase of distance between pillars d. Note that the ATS in our case exists only for $d < 1.4a$, therefore the transition region $d \in [1.4a, 1.8a]$ as well as the larger distances other than the AIT regions do not represent ATS or AIT. We can see that the theoretical distinction between ATS and AIT helps the comprehension of the analytical results. On the other hand, this criterion is useful when we cannot theoretically rule out the AIT phenomenon. This happens, for example, when the radius mismatch is so large that the peak is much wider with respect to the two dips. In this case, although FP resonance is still present between two dips, the transmission spectra can not be well fitted by the AIT model and therefore cannot be ascribed to an AIT.

The above effects can also be obtained by detuning the pillar height. The heights of the two pillars are increased or reduced from the original height $h = 0.6a$ by the same amount Δh. That is, $h_1 = h + \Delta h$ and $h_2 = h - \Delta h$. The radius of both the two pillars r_1 and r_2 are fixed at $0.2a$. Figure 14 shows the transmission spectra of Love waves through the two lines of pillars when $d = 2a$, i.e., in the region of AIT. It can be seen that by decreasing Δh, the two dips approach each other and the peak with almost unchanged frequency decreases and becomes invisible for identical pillars.

VI. CONCLUSION

In this work, the interaction of Love waves with two lines of cylindrical Ni pillars is investigated on a silica film deposited on a 90ST quartz substrate. Firstly, pillar intrinsic torsional mode is demonstrated to be well excited by Love waves. One line of pillars can give rise to a sharp transmission dip due to a destructive interference. Secondly, the acoustic analog of ATS and Fabry-Perot resonance of Love waves are demonstrated in two lines of identical pillars by varying the distance between the pillar lines. ATS appears when the distance is smaller than the half wavelength and a strong coupling is aroused between the pillar lines, causing the pillar-mode-induced transmission dip to split into two dips with a transparency window in the middle. This coupling decreases with the increase of pillar distance. We demonstrate the different pillar vibration symmetries at the two dip frequencies, which lead to different dip widths. Fabry-Perot resonance exists at the positions where the distance between the pillar lines is a multiple of half wavelength. The proximity of Fabry-Perot

resonance with pillar intrinsic mode gives rise to the cavity modes with transmission enhancement on the two edges of the single dip. We avoid mixing up the FP resonances with the cavity modes by presenting the different frequency variation with respect to the distance between the pillars. Thirdly, the radius of one line of the pillar is modified to detune the pillar resonant frequency. In the pillar-coupling region, the coupling effect decreases with the increase of radius mismatch, and the two dips rejoin their individual pillar-mode frequencies. When the distance between the pillar lines is a multiple of half wavelength, Fabry-Perot resonance along with the two different pillars' resonances give rise to the AIT. The same phenomena can also be obtained by detuning the pillar height. Then, with a similar transparency window in the transmission spectra, ATS and AIT phenomena are first fitted with the corresponding formula models, showing good agreements. The fit parameters are demonstrated as functions of the geometrical parameter. The AIC is then used to quantitatively evaluate the quality of the fit models, which illustrates the transition from ATS to AIT as well as the periodicity of AIT by increasing the distance between the pillar lines. The theoretical and analytical differentiation of ATS and AIT should be used together to discriminate the assignment of the observed spectrum to one or the other physical mechanisms. The results presented in this study could be used for potential acoustic applications such as wave control, metamaterials, and biosensors.

APPENDIX A: DISSIPATION CONSIDERATION

To consider the losses by dissipation, we recalculate the critical transmission curves by changing Young's modulus E of the silica film and the pillars to complex numbers $E(1+j\epsilon)$, with ϵ equal to 5×10^{-4} and 1×10^{-3}. Corresponding transmission spectra for different phenomena (dips, ATS, cavity modes, and AIT) are shown in Fig. 15. It can be seen that all the main resonances and dips are visible for ϵ below 1×10^{-3}. With $\epsilon=1\times10^{-3}$, we can estimate a propagation length around 2 mm. In experiments, Love waves can propagate for a few mm. We have already realized 500-MHz devices with distances between the transmitter and receiver of a few mm [66]. This means the parameter ϵ is below 1×10^{-3}, which indicates that our system is robust for practical applications.

APPENDIX B: CAVITY MODE AND FP RESONANCE

1. Two lines of identical pillars

In order to show the behavior of the cavity modes at the vicinity of the transmission dip, we plot, in Fig. 16(a), the transmission spectra for $d=2.4a$ when all the pillars' radii vary from $0.196a$ to $0.204a$. It can be seen that we obtain almost the same cavity mode besides the dip at different frequencies. Along with Figs. 6(b) and 16(a), we can present in Fig. 16(b) the relation between cavity modes (black lines) and FP resonance (red line). When we change the pillar resonant frequency (blue lines), FP resonance remains at almost the same position. For each radius value,

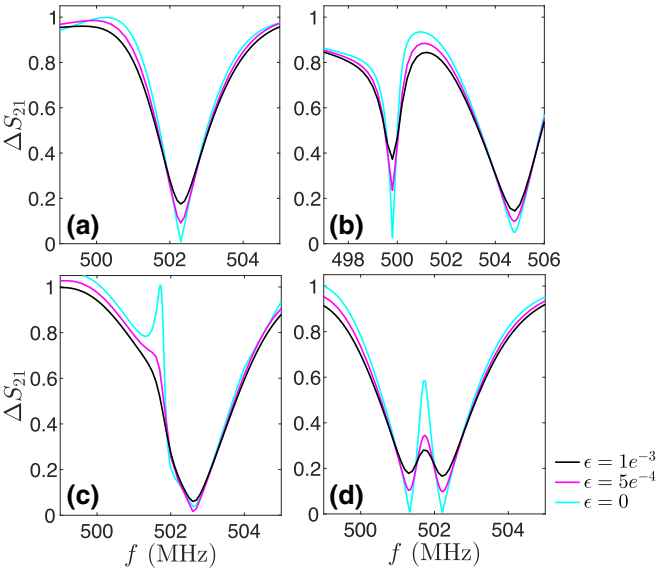

FIG. 15. (a) Transmission dip for a single-pillar line with $r=0.2a$; (b) ATS for two lines of identical pillars with $r_{1,2}=0.2a$; (c) Cavity mode for two lines of identical pillars with $r_{1,2}=0.2a$; (d) AIT for two lines of dissimilar pillars with $r_1=0.2a$ and $r_2=0.202a$. $a=2$ μm. Cyan curves are the transmission without dissipation. Rose and black curves correspond to the transmission with $\epsilon=5\times10^{-4}$ and 1×10^{-3}, respectively.

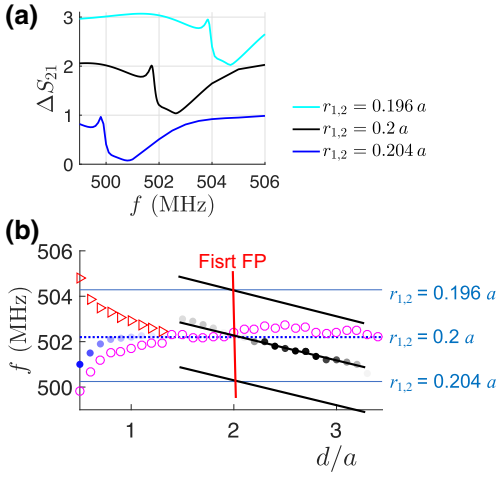

FIG. 16. (a) Transmission spectra for $d=2.4a$ when all the pillars' radii vary from $0.196a$ to $0.204a$. (b) Cavity modes (black lines) for two lines of identical pillars when changing the pillar resonant frequency (blue lines). Red line denotes the first FP resonance.

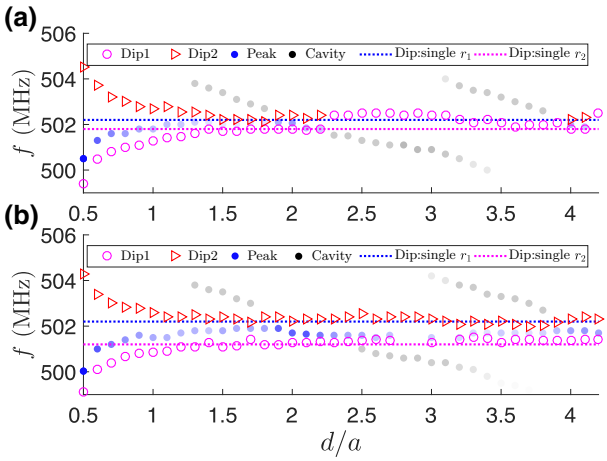

FIG. 17. Frequencies of dips, peaks, and cavity modes as a function of the distance d between two dissimilar pillar lines, in the case of (a) $r_1 = 0.2a$ and $r_2 = 0.201a$, and (b) $r_1 = 0.2a$ and $r_2 = 0.202a$. $a = 2\ \mu$m.

the FP resonance is a particular case of the cavity modes when the later coincide with the dip.

2. Two lines of dissimilar pillars

Figure 17 gives the same results as in Fig. 7, but with two lines of dissimilar pillars. Figure 17(a) is the case of $r_1 = 0.2a$ and $r_2 = 0.201a$. Dip1 (dip2) corresponds to the second (first) pillar. It can be seen that outside the ATS region, dip2 becomes invisible after d exceeds $2.2a$. This is because on the one hand, the interaction between the two pillars becomes too weak and on the other hand, the radius mismatch is too small. This dip becomes visible again when d approaches $4a$, since the interaction between the two pillars regains its strength in the AIT region. When we enlarge the radius difference [see Fig. 17(b)], most of dip1 in this region becomes visible. Moreover, we can see that the cavity modes cross the center of the two dips at $d = 2a$ and $4a$, where we obtain the AIT resonance of FP type. This behavior is compatible with the cavity mode-FP resonance relation that we present in Fig. 16(b). FP resonances are particular cases of the cavity modes when the later fall between the two dips.

[1] M. Fleischhauer, A. Imamoglu, and J. P. Marangos, Electromagnetically induced transparency: Optics in coherent media, Rev. Mod. Phys. **77**, 633 (2005).

[2] L. V. Hau, S. E. Harris, Z. Dutton, and C. H. Behroozi, Light speed reduction to 17 metres per second in an ultracold atomic gas, Nature **397**, 594 (1999).

[3] H. M. M. Alotaibi and B. C. Sanders, Enhanced nonlinear susceptibility via double-double electromagnetically induced transparency, Phys. Rev. A **94**, 053832 (2016).

[4] G. Heinze, C. Hubrich, and T. Halfmann, Phys. Rev. Lett. **111**, 033601 (2013).

[5] S. H. Autler and C. H. Townes, Stark effect in rapidly varying fields, Phys. Rev. J. Arch. **100**, 703 (1955).

[6] T. Y. Abi-Salloum, Electromagnetically induced transparency and Autler-Townes splitting: Two similar but distinct phenomena in two categories of three-level atomic systems, Phys. Rev. A **81**, 053836 (2010).

[7] K. J. Boller, A. Imamoglu, and S. E. Harris, Observation of Electromagnetically Induced Transparency, Phys. Rev. Lett. **66**, 2593 (1991).

[8] B. Peng, S. K. Ozdemir, W. Chen, F. Nori, and L. Yang, What is and what is not electromagnetically induced transparency in whispering-gallery microcavities, Nat. Commun. **5**, 5082 (2014).

[9] Y.-C. Liu, B.-B. Li, and Y.-F. Xiao, Electromagnetically induced transparency in optical microcavities, Nanophotonics **6**, 789 (2017).

[10] B. Wei and S. Jian, Objectively discriminating the optical analogy of electromagnetically induced transparency from Autler-Townes splitting in a side coupled graphene-based waveguide system, J. Opt. **19**, 115001 (2017).

[11] C. Dong, V. Fiore, M. C. Kuzyk, and H. Wang, Optomechanical dark mode, Science **21**, 1609 (2012).

[12] A. H. Safavi-Naeini, T. P. Mayer Alegre, J. Chan, M. Eichenfield, M. Winger, Q. Lin, J. T. Hill, D. E. Chang, and O. Painter, Electromagnetically induced transparency and slow light with optomechanics, Nature **472**, 69 (2011).

[13] S. Weis, R. Riviere, S. Deleglise, E. Gavartin, O. Arcizet, A. Schliesser, and T. J. Kippenberg, Optomechanically induced transparency, Science **330**, 1520 (2010).

[14] S. Zhang, D. A. Genov, Y. Wang, M. Liu, and X. Zhang, Plasmon-induced Transparency in Metamaterials, Phys. Rev. Lett. **101**, 047401 (2008).

[15] N. Liu, L. Langguth, T. Weiss, J. Kastel, M. Fleischhauer, T. Pfau, and H. Giessen, Plasmonic analogue of electromagnetically induced transparency at the Drude damping limit, Nat. Mater. **8**, 758 (2009).

[16] Z. Han and S. I. Bozhevolnyi, Plasmon-induced transparency with detuned ultracompact Fabry-Perot resonators in integrated plasmonic devices, Opt. Express **19**, 3251 (2011).

[17] N. Liu, T. Weiss, M. Mesch, L. Langguth, U. Eigenthaler, M. Hirscher, C. Sonnichsen, and H. Giessen, Planar metamaterial analogue of electromagnetically induced transparency for plasmonic sensing, Nano Lett. **10**, 1103 (2010).

[18] J. Gu, R. Singh, X. Liu, X. Zhang, Y. Ma, S. Zhang, S. A. Maier, Z. Tian, A. K. Azad, H.-T. Chen, A. J. Taylor, J. Han, and W. Zhang, Active control of electromagnetically induced transparency analogue in terahertz metamaterials, Nat. Commun. **3**, 1151 (2012).

[19] N. Papasimakis, V. A. Fedotov, N. I. Zheludev, and S. L. Prosvirnin, Metamaterial Analog of Electromagnetically Induced Transparency, Phys. Rev. Lett. **101**, 253903 (2008).

[20] P. M. Anisimov, J. P. Dowling, and B. C. Sanders, Objectively Discerning Autler-Townes Splitting from Electromagnetically Induced Transparency, Phys. Rev. Lett. **107**, 163604 (2011).

[21] H.-C. Sun, Y.-X. Liu, H. Ian, J. Q. You, E. Il'ichev, and F. Nori, Electromagnetically induced transparency and Autler-Townes splitting in superconducting flux quantum circuits, Phys. Rev. A **89**, 063822 (2014).
[22] J. Liu, H. Yang, C. Wang, K. Xu, and J. Xiao, Experimental distinction of Autler-Townes splitting from electromagnetically induced transparency using coupled mechanical oscillators system, Sci. Rep. **6**, 19040 (2016).
[23] L. Giner, L. Veissier, B. Sparkes, A. Sheremet, A. Nicolas, O. S. Mishina, M. Scherman, S. Burks, I. Shomroni, D. V. Kupriyanov, P. K. Lam, E. Giacobino, and J. Laurat, Experimental investigation of the transition between Autler-Townes splitting and electromagnetically-induced-transparency models, Phys. Rev. A **87**, 013823 (2013).
[24] C. Zhu, C. Tan, and G. Huang, Crossover from electromagnetically induced transparency to Autler-Townes splitting in open V-type molecular systems, Phys. Rev. A **87**, 043813 (2013).
[25] C. Tan and G. Huang, Crossover from electromagnetically induced transparency to Autler-Townes splitting in open ladder systems with Doppler broadening, J. Opt. Soc. Am. B **31**, 704 (2014).
[26] Y. V. Radeonychev, M. D. Tokman, A. G. Litvak, and O. Kocharovskaya, Acoustically Induced Transparency in Optically Dense Resonance Medium, Phys. Rev. Lett. **96**, 093602 (2006).
[27] F. Liu, M. Ke, A. Zhang, W. Wen, J. Shi, Z. Liu, and P. Sheng, Acoustic analog of electromagnetically induced transparency in periodic arrays of square rods, Phys. Rev. E **82**, 026601 (2010).
[28] A. Santillan and S. I. Bozhevolnyi, Acoustic transparency and slow sound using detuned acoustic resonators, Phys. Rev. B **84**, 064304 (2011).
[29] M. Amin, A. Elayouch, M. Farhat, M. Addouche, A. Khelif, and H. Bagci, Acoustically induced transparency using Fano resonant periodic arrays, J. Appl. Phys. **118**, 093602 (2015).
[30] I. Quotane, E. H. El Boudouti, and B. Djafari-Rouhani, Trapped-mode-induced Fano resonance and acoustical transparency in a one-dimensional solid-fluid phononic crystal, Phys. Rev. B **97**, 024304 (2018).
[31] Y. Jin, Y. Pennec, and B. Djafari-Rouhani, Acoustic analogue of electromagnetically induced transparency and Autler-Townes splitting in pillared metasurfaces, J. Phys. D: Appl. Phys. **51**, 494004 (2018).
[32] R. Martínez-Sala, J. Sancho, J. V. Sánchez, V. Gómez, J. Llinares, and F. Meseguer, Sound attenuation by sculpture, Nature **378**, 241 (1995).
[33] Z. Liu, X. Zhang, Y. Mao, Y. Y. Zhu, Z. Yang, C. T. Chan, and P. Sheng, Locally resonant sonic materials, Science **289**, 1734 (2000).
[34] A. Khelif, A. Choujaa, B. Djafari-Rouhani, M. Wilm, S. Ballandras, and V. Laude, Trapping and guiding of acoustic waves by defect modes in a full-band-gap ultrasonic crystal, Phys. Rev. B **68**, 214301 (2003).
[35] Y. Pennec, J. O. Vasseur, B. Djafari-Rouhani, L. Dobrzyński, and P. A. Deymier, Two-dimensional phononic crystals: Examples and applications, Surf. Sci. Rep. **65**, 229 (2010).
[36] J. Zhu, J. Christensen, J. Jung, L. Martin-Moreno, X. Yin, L. Fok, X. Zhang, and F. J. Garcia-Vidal, A holey-structured metamaterial for acoustic deep-subwavelength imaging, Nat. Phys. **7**, 52 (2011).
[37] L. Yang, N. Yang, and B. Li, Extreme low thermal conductivity in nanoscale 3D Si phononic crystal with spherical pores, Nano Lett. **14**, 1734 (2014).
[38] Z. Xu and Y. J. Yuan, Implementation of guiding layers of surface acoustic wave devices: A review, Biosens. Bioelectron. **99**, 500 (2018).
[39] T.-C. Wu, T.-T. Wu, and J.-C. Hsu, Waveguiding and frequency selection of Lamb waves in a plate with a periodic stubbed surface, Phys. Rev. B **79**, 104306 (2009).
[40] B. Liang, X. S. Guo, J. Tu, D. Zhang, and J. C. Cheng, An acoustic rectifier, Nat. Mater. **9**, 989 (2010).
[41] F. Meseguer, M. Holgado, D. Caballero, N. Benaches, J. Sánchez-Dehesa, C. López, and J. Llinares, Rayleigh-wave attenuation by a semi-infinite two-dimensional elastic-band-gap crystal, Phys. Rev. B **59**, 12169 (1999).
[42] R. H. Olsson III and I. El-Kady, Microfabricated phononic crystal devices and applications, Meas. Sci. Technol. **20**, 012002 (2009).
[43] L. Binci, C. Tu, H. Zhu, and J. E.-Y. Lee, Planar ring-shaped phononic crystal anchoring boundaries for enhancing the quality factor of Lamb mode resonators, Appl. Phys. Lett. **109**, 203501 (2016).
[44] A. Talbi, F. Sarry, M. Elhakiki, L. L. Brizoual, O. Elmazria, P. Nicolay, and P. Alnot, ZnO/quartz structure potentiality for surface acoustic wave pressure sensor, Sens. Actuat. A: Phys. **128**, 78 (2006).
[45] M. Ke, M. Zubtsov, and R. Lucklum, Sub-wavelength phononic crystal liquid sensor, J. Appl. Phys. **110**, 026101 (2011).
[46] A. Salman, O. A. Kaya, A. Cicek, and B. Ulug, Low-concentration liquid sensing by an acoustic Mach–Zehnder interferometer in a two-dimensional phononic crystal, J. Phys. D: Appl. Phys. **48**, 255301 (2015).
[47] J.-K. Yu, S. Mitrovic, D. Tham, J. Varghese, and J. R. Heath, Reduction of thermal conductivity in phononic nanomesh structures, Nat. Nanotechnol. **5**, 718 (2010).
[48] N. Zen, T. A. Puurtinen, T. J. Isotalo, S. Chaudhuri, and I. J. Maasilta, Engineering thermal conductance using a two-dimensional phononic crystal, Nat. Commun. **5**, 3435 (2014).
[49] X. Zhang and Z. Liu, Negative refraction of acoustic waves in two-dimensional phononic crystals, Appl. Phys. Lett. **85**, 341 (2004).
[50] D. M. Profunser, E. Muramoto, O. Matsuda, O. B. Wright, and U. Lang, Dynamic visualization of surface acoustic waves on a two-dimensional phononic crystal, Phys. Rev. B **80**, 014301 (2009).
[51] S. Narayana and Y. Sato, Heat Flux Manipulation with Engineered Thermal Materials, Phys. Rev. Lett. **108**, 214303 (2012).
[52] J. Li, F. Wu, H. Zhong, Y. Yao, and X. Zhang, Acoustic beam splitting in two-dimensional phononic crystals using self-collimation effect, J. Appl. Phys. **118**, 144903 (2015).
[53] Y. Guo, D. Brick, M. Großmann, M. Hettich, and T. Dekorsy, Acoustic beam splitting at low GHz frequencies in a

defect-free phononic crystal, Appl. Phys. Lett. **110**, 031904 (2017).

[54] P.-C. Li, Y. Zhao, A. Alu, and E. T. Yu, Experimental realization and modeling of a subwavelength frequency-selective plasmonic metasurface, Appl. Phys. Lett. **99**, 221106 (2011).

[55] N. Yu and F. Capasso, Flat optics with designer metasurfaces, Nat. Mater. **13**, 139 (2014).

[56] M. Oudich, B. Djafari-Rouhani, B. Bonello, Y. Pennec, S. Hemaidia, F. Sarry, and D. Beyssen, Rayleigh Waves in Phononic Crystal Made of Multilayered Pillars: Confined Modes, Fano Resonances, and Acoustically Induced Transparency, Phys. Rev. Appl. **9**, 034013 (2018).

[57] Y. Jin, E. H. El Boudouti, Y. Pennec, and B. Djafari-Rouhani, Tunable Fano resonances of Lamb modes in a pillared metasurface, J. Phys. D: Appl. Phys. **50**, 425304 (2017).

[58] Y. Jin, B. Bonello, R. P. Moiseyenko, Y. Pennec, O. Boyko, and B. Djafari-Rouhani, Pillar-type acoustic metasurface, Phys. Rev. B **96**, 104311 (2017).

[59] Y. Liu, A. Talbi, B. Djafari-Rouhani, E. H. El Boudouti, L. Dobohlavova, V. Mortet, O. Bou Matar, and P. Pernod, Interaction of Love waves with coupled cavity modes in a 2D Holey phononic crystal, Phys. Lett. A **383**, 1502 (2019).

[60] R. Lucklum and J. Li, Phononic crystals for liquid sensor applications, Meas. Sci. Technol. **20**, 124014 (2009).

[61] T.-W. Liu, Y.-C. Lin, Y.-C. Tsai, T. Ono, S. Tanaka, and T.-T. Wu, Evidence of a Love wave bandgap in a quartz substrate coated with a phononic thin layer, Appl. Phys. Lett. **104**, 181905 (2014).

[62] T.-W. Liu, Y.-C. Tsai, Y.-C. Lin, T. Ono, S. Tanaka, and T.-T. Wu, Design and fabrication of a phononic-crystal-based Love wave resonator in GHz range, AIP Adv. **4**, 124201 (2014).

[63] Y. Liu, A. Talbi, P. Pernod, and O. Bou Matar, Highly confined Love waves modes by defect states in a holey SiO/quartz phononic crystal, J. Appl. Phys. **124**, 145102 (2018).

[64] S. Yankin, A. Talbi, Y. Du, J.-C. Gerbedoen, V. Preobrazhensky, P. Pernod, and O. Bou Matar, Finite element analysis and experimental study of surface acoustic wave propagation through two-dimensional pillar-based surface phononic crystal, J. Appl. Phys. **115**, 244508 (2014).

[65] K. P. Burnham and D. R. Anderson, eds., *Model Selection and Multimodel Inference* (Springer-Verlag, New York, 2002), 2nd ed.

[66] A. Talbi, A. Soltani, A. Rumeau, A. Taylor, L. Drbohlavova, L. Klimsa, J. Kopecek, L. Fekete, M. Krecmarova, and V. Mortet, Simulations, fabrication, and characterization of diamond-coated Love wave-type surface acoustic wave sensors, Phys. Status Solidi A Appl. Mater. Sci. **212**, 2606 (2015).